Ultrahigh Surface Area Hierarchically Porous Carbon Materials from Polyacrylamide-cellulose Hydrogel for High-performance Supercapacitors

Nadiia Velychkivska,[†,¶,*] *Anna Golunova,*[¶] *Atanu Panda,*[†] *Pragati A. Shinde,*[†] *Renzhi Ma,*[†] *Katsuhiko Ariga,*[†,‡] *Yusuke Yamauchi,* [$,⊥,±] *Jonathan P. Hill,*[†,*] *Jan Labuta,*[†,*] *and Lok Kumar Shrestha*[†,#,*]

[†]Research Center for Materials Nanoarchitectonics (MANA), National Institute for Materials Science (NIMS), 1-1 Namiki, Tsukuba, Ibaraki 305-0044, Japan
[¶]Institute of Macromolecular Chemistry, AS CR, Heyrovsky Sq. 2, 162 06 Prague 6, Czech Republic
[‡]Department of Advanced Materials Science, Graduate School of Frontier Sciences, The University of Tokyo, 5-1-5 Kashiwanoha, Kashiwa 277-8561, Chiba, Japan
[$]Australian Institute for Bioengineering and Nanotechnology, The University of Queensland, Brisbane, Queensland 4072, Australia
[⊥]Department of Materials Process Engineering, Graduate School of Engineering, Nagoya University, Nagoya, Japan
[±]Department of Chemical and Biomolecular Engineering, Yonsei University, 50 Yonsei-ro, Seodaemun-gu, Seoul 03722, South Korea
[#]Department of Materials Science, Faculty of Pure and Applied Sciences, University of Tsukuba 1-1-1, Tennodai, Tsukuba 305-8573, Ibaraki, Japan

*Corresponding authors: Nadiia Velychkivska (Email: velychkivska.nadiia@nims.go.jp),
Jonathan P. Hill (Email: jonathan.hill@nims.go.jp),
Jan Labuta (Email: LABUTA.Jan@nims.go.jp), and
Lok Kumar Shrestha (Email: SHRESTHA.Lokkumar@nims.go.jp)

ABSTRACT. High surface area, hierarchically micro-mesoporous carbon materials with interconnected pore structures have significant potential as electrode materials for high-performance supercapacitor applications. Here, we present the synthesis of ultrahigh surface area hierarchically porous carbon materials, prepared by potassium carbonate (K_2CO_3) activation of polyacrylamide-hydroxy propyl cellulose (PAM-HPC) hydrogel at high temperatures (500−900 °C), and their energy storage performances in two- and three-electrode cell set-up. The carbon material obtained by carbonization of PAM-HPC hydrogel at 800 °C exhibits an ultrahigh surface area of 3387.2 $m^2\ g^{-1}$ with a large pore volume of 1.963 $cm^3\ g^{-1}$. The electrode prepared using this material demonstrated excellent supercapacitance performance in the three-electrode system, achieving a high specific capacitance of 545.5 F g^{-1} at 1 A g^{-1} current density with superior rate capability and outstanding cycling stability of 96.3% after 5000 charge-discharge cycles. Furthermore, the assembled symmetric supercapacitor device constructed using this material showed a high specific capacitance of 102.5 F g^{-1} at 0.5 A g^{-1}. It delivers a high energy density of 17.2 Wh kg^{-1} at the power density of 550 W kg^{-1}, and superior cycling stability of 94.2% after 5000 consecutive charge-discharge cycles. The electrochemical properties reported here indicate that hierarchically porous carbons obtained from PAM-HPC hydrogels are promising materials for high-performance supercapacitor applications.

KEYWORDS: Polyacrylamide, cellulose, hydrogel, hierarchically porous carbon, EDLC, supercapacitor

INTRODUCTION

In the prevailing worldwide decarbonization economy, a burgeoning demand for materials having efficient energy storage and energy conversion features has emerged. To establish an

energy-sustainable society, supercapacitors could make an invaluable contribution based on their extremely high power densities, remarkable rate and cycle life performances, and economical fabrication costs.[1-3] Supercapacitors are categorized as electrical double-layer capacitors (EDLCs), pseudocapacitors, and hybrid supercapacitors depending on the mechanism of energy storage.[4-6] EDLCs use a non-faradaic mechanism and store energy electrostatically without charge transfer between electrodes and electrolyte.[7] Pseudocapacitors utilize a reversible faradaic energy storage mechanism based on redox reactions at and near the electrode-electrolyte interface.[8] Hybrid supercapacitors combine the properties of EDLCs and pseudocapacitors. In order to obtain an effective supercapacitor device, the electrode material must be carefully selected. For this purpose, highly porous carbon materials show sufficient electrochemical performance due to a well-defined hierarchical arrangement of micro, meso, and macropores, exhibit excellent stability, and have appropriate electrical conductivity. Various nanocarbon materials, such as activated carbon,[9,10] carbon nanotubes,[11,12] graphene-based carbon materials,[13,14] and carbide-derived carbons[15] have been used widely as electrode materials in supercapacitors. Investigations have revealed that porosity plays a critical role in improving energy storage performance. However, the task of producing ultrahigh surface area hierarchically porous carbon materials for the enhancement of supercapacitor performance remains challenging.

Porosity of carbon materials can be modulated by physical or chemical activation of the starting materials. Generally, chemical activation is more effective than physical activation since it leads to the synthesis of ultrahigh surface area carbon materials.[16] Activators including alkali or alkaline earth metal salts and other compounds (KOH, K_2CO_3, NaOH, $ZnCl_2$, H_3PO_4) have been commonly applied for chemical activation.[17] Potassium carbonate, K_2CO_3, is one of the most effective chemical activators since it decomposes generating CO_2, which leads to the formation of

micro/meso pores within the carbon structure during the carbonization process; the mechanism of chemical activation has been previously reported in the literature.[18] Above 700 °C, potassium carbonate decomposes to K_2O and CO_2 gas or reacts directly with carbon forming K metal and CO gas, Eq. 1, 2 and 3. Potassium oxide can also react with carbon and produce metallic K and CO gas. The released gaseous products exfoliate the carbon sheets, whereas metallic potassium or its oxide creates pores in the carbon structure due to their elimination during annealing and washing procedures.[19]

$$K_2CO_3 = K_2O + CO_2 \quad (1)$$
$$K_2CO_3 + 2C = 2K + 3CO \quad (2)$$
$$K_2O + C = 2K + CO \quad (3)$$

Highly porous carbonaceous materials can be obtained from natural (biomass) or synthetic carbon sources.[2,17] Unlike biomass-derived carbon materials, whose composition differs depending on their origin, synthetic carbon materials offer morphological tunability, reproducibility, cost-efficiency, and simple preparation techniques. Of these, hydrogel-derived carbon materials have recently emerged as materials for energy-related applications because of their adjustable physicochemical properties.[20] For example, chemically activated cellulose-derived carbon aerogels with well-developed hierarchical pore structures and high specific capacitance values have been reported.[21,22] However, in order to acquire high-performance supercapacitors, surface chemistry and pore distribution should be effectively tuned. Previous research has shown that heteroatom doping of the carbon precursors, usually with nitrogen and oxygen, promotes the wettability of electrode surfaces, increases electrical conductivity, and improves the specific capacitance of an electrode due to pseudocapacitive behavior[7,23-32] so that the use of a self-doped nitrogen-rich precursor for carbon electrodes is an effective means to obtain highly functional materials for supercapacitors. Polyacrylamide (PAM) hydrogel having a network of

polyacrylamide units (-CH_2-CH-CO-NH_2-) covalently bonded using a crosslinking agent is a potential and suitable candidate for this purpose. Zhang et al.[33] obtained a high capacitance carbon material (238.2 F g^{-1} at 2 A g^{-1}) derived from PAM hydrogel activated by applying zinc metal. The capacitance of the material was increased 2.86 times by the incorporation of redox additive sodium p-aminobenzenesulfonate into the KOH electrolyte. Wu et al.[34] prepared a nitrogen-doped porous carbon material having a large specific capacitance (302.1 F g^{-1} at 1 A g^{-1}in 6 M KOH) from PAM hydrogel activated by using KOH. Polyacrylamide-derived carbon activated with calcium acetate has a specific capacitance of 194.7 F g^{-1} at 0.5 A g^{-1} in 6 M KOH.[35] A large specific capacitance (346.9 F g^{-1} 0.5 A g^{-1} in 3 M KOH) and good rate capability (224.4 F g^{-1} at 50 A g^{-1}) of nitrogen-doped porous carbon materials have also been attained using PAM hydrogel with carboxymethylcellulose. In that case, the material was templated and activated by using K_2CO_3 and/or $K_2B_4O_7$, which allowed tuning of porosity leading to a material having a large specific surface area.[36] PAM-glucose hydrogel-derived carbon activated by KOH[37] showed a high specific capacitance (441 F g^{-1} at 0.25 A g^{-1} in 6 M KOH). However, although PAM hydrogel-derived carbon materials are promising electrode materials for energy storage applications, there are only a few reports of their use for this purpose.

In this work, we present the synthesis and electrochemical performances of intrinsically N, O-doped polyacrylamide-hydroxypropyl cellulose (PAM-HPC) hydrogel-derived carbon materials with ultrahigh surface areas and hierarchically developed micro-mesopore architectures as electrodes for supercapacitors. Porosity was regulated based on carbonization temperature, the presence (or absence) of a chemical activator (K_2CO_3), and hydrogel concentration. The fabrication method is economical and effective, and benefits from the use of both synthetic and natural polymers. A (co)polymerization/crosslinking reaction between acrylamide

(carbon/nitrogen source), hydroxypropyl cellulose (carbon/oxygen source), and a crosslinker (N,N′-methylenebiacrylamide) with homogenous in situ incorporation of the activator is followed by freeze-drying of the resulting hydrogel, then carbonization at high temperature (500-900 °C) in an inert nitrogen atmosphere. The carbon material obtained by annealing at 800 °C has an ultrahigh surface area (3387.2 m^2 g^{-1}), hierarchical micro- and mesoporosity with nitrogen and oxygen surface functionalities. The electrode prepared using this material has a remarkable specific capacitance of 545.5 F g^{-1} at 1 A g^{-1} in 1 M H_2SO_4 aqueous electrolyte solution a three-electrode system with outstanding cycle performance of 96.3% after 5000 cycles. Additionally, a symmetric supercapacitor cell assembled using the electrode reached a specific capacitance value of 102.5 F g^{-1} at 0.5 A g^{-1}. The device achieved a high energy density of 17.2 Wh kg^{-1} at the power density of 550 W kg^{-1} with an excellent cycle life of 94.2% after 5000 charging-discharging cycles, demonstrating that polyacrylamide-cellulose (PAM-HPC) hydrogel-derived nanoporous carbon materials have substantial potential in high-performance supercapacitor applications.

EXPERIMENTAL SECTION

Materials. Acrylamide (AM), potassium persulfate ($K_2S_2O_8$), and sodium sulfite (Na_2SO_3) were purchased from Wako Pure Chemical Industries, Tokyo, Japan. N,N′-methylenebiacrylamide (MBA) was purchased from Tokyo Chemical Industry, Tokyo, Japan. Potassium carbonate (K_2CO_3) was purchased from Nacalai Tesque, Kyoto, Japan. Hydroxypropyl cellulose (HPC) was purchased from Sigma Aldrich, Darmstadt, Germany. All of the compounds were used as received unless stated otherwise. Deionized water (H_2O) was used for hydrogel preparation.

Preparation of porous carbon materials from PAM-HPC hydrogel. PAM-HPC was synthesized according to a literature procedure[36] with minor modifications. AM (360 mg), MBA (40 mg), K_2CO_3 (500 mg) were loaded into a 30 mL-capacity glass vial. Deionized water (3 mL)

and HPC solution (5 g; 2 wt%) were then added. The mixture was stirred with cooling in an ice-water bath until complete dissolution of the solid materials then sparged with nitrogen gas for 30 minutes to remove oxygen, which can inhibit the free radical (co)polymerization reaction between AM and MBA. Na_2SO_3 (10 mg) and $K_2S_2O_8$ (20 mg) were each dissolved in deionized water (1 mL) then injected into the deoxygenated reaction mixture to initiate the free radical (co)polymerization reaction. The mixture was shaken vigorously and then incubated for 2 h at 25 °C. Gelation commenced within the first few minutes. The free radical (co)polymerization reaction results in a semi-interpenetrated polymer network (SIPN) of polyacrylamide (PAM) and hydroxypropyl cellulose (HPC) polymer, which forms a stable hydrogel in water. The hydrogel was frozen in liquid nitrogen (which leads to rapid macropore formation) and then dried in a freeze drier (EYELA FDU-1200, Tokyo, Japan) for 48 h. Following freeze-drying, samples of the dried hydrogel were subjected to heat treatment for carbonization at different temperatures for 2 h under N_2 gas flow (120 cm^3 min^{-1}) at a heating rate of 10 °C min^{-1}. Heat treatment was performed using a tube furnace (KOYO, Tokyo, Japan). The resulting carbonized samples were washed thoroughly with deionized water until neutral pH was reached and dried in a vacuum oven at 80 °C. The samples are referred to according to their compositions as follows: PAM_x-HPC-KY, where x is the concentration of hydrogel (2, 4 or 8 wt%), Y is the carbonization temperature (500, 700, 800, 900 °C) and K indicates the use of the chemical activation agent (K_2CO_3). For PAM_4, the quantities described above were used. For PAM_2, AM (180 mg) and MBA (20 mg) were used while for PAM_8, AM (720 mg) and MBA (80 mg) were used. The amount of K_2CO_3 and HPC solution added to the reaction mixtures was the same in each case.

Material characterizations. Thermogravimetric analyses (TGA) of PAM-HPC carbon materials were carried out using STA 2500 (Regulus, Netzsch, Wittelsbacherstraße, SELB,

Germany) at a sample heating rate of 10 °C min^{-1} under a nitrogen atmosphere. PAM-HPC carbons were characterized by Raman scattering spectroscopy at the excitation wavelength of neon laser 532.09 nm (NRS-3100, JASCO, Tokyo, Japan). Powder X-ray diffraction (XRD) patterns of the PAM-HPC carbon materials were collected at V = 40 kV and I = 30 mA with Cu-Kα radiation at 25 °C in the scan range of 2θ = 5−80° using Rigaku X-ray diffractometer (RINT, Tokyo, Japan). Surface compositions of PAM-HPC carbon materials were studied by using X-ray photoelectron spectroscopy (XPS) (Quantera SXM instrument, ULVAC-PHI, Chanhassen, MN, USA). The identities of oxygen and nitrogen functional groups in PAM-HPC carbon samples were examined by using Fourier-transform infrared (FTIR) spectroscopy, NICOLET iS20 instrument (Thermo-Fisher Scientific, Waltham, MA, USA). Surface morphologies of the carbon materials were investigated by using scanning electron microscopy (SEM: S-4800, Hitachi Co., Ltd., Japan, operated at an accelerating voltage of 10 kV) and transmission electron microscopy (TEM) using a JEM2100F instrument (JEOL, Tokyo, Japan) operated at 200 kV. In order to minimize charging effects during imaging, samples for SEM were coated with platinum (~2 nm) using a Hitachi S-2030 ion coater prior to observation. Textural properties of PAM-HPC carbons, i.e., Brunauer−Emmett−Teller (BET) surface area and porosity, were studied by nitrogen adsorption isotherms recorded at 77 K (Quantachrome Autosorb-iQ2, Boynton Beach, FL, USA). Prior to adsorption/desorption measurements, samples (15-20 mg) were loaded into a glass cell followed by degassing at 120 °C for 24 h. The Barrett−Joyner−Halenda (BJH) and density functional theory (DFT) methods provided information about the pore dimensions and pore volumes.

Electrochemical measurements. The applicability of PAM-HPC carbon materials for supercapacitor applications was evaluated by cyclic voltammetry (CV), galvanostatic charge−discharge (GCD), and electrochemical impedance spectroscopy (EIS) measurements.

Electrochemical measurements were performed in a three-electrode system with an aqueous electrolyte (1 M H_2SO_4, 25 °C) using an ALS CHI 660E workstation (CH Instruments, Inc. Austin, TX, USA). Working electrodes were prepared on glassy carbon electrodes (GCE). Carbon material (2 mg) was dispersed in water:ethanol mixture (1 mL, 4:1 v/v) then sonicated for 1 h. The suspension obtained (3 μL) was drop-casted at the center of the GCE followed by drying for 1 h at 70 °C to remove the solvents. The carbon material was then coated with Nafion (5 μL, 0.5 wt.% in ethanol) on the GCE and then dried under reduced pressure for 24 h at 70 °C. The mass of the active material for each electrode was 6×10^{-3} mg. A platinum wire and Ag/AgCl were used as the counter-and reference electrode, respectively. EIS measurements were performed in the frequency range of 0.01 Hz−100 kHz at an amplitude of 5 mV. Specific capacitances (C_s, F g^{-1}) were calculated from the GCD curves according to Eq. 4:

$$C_s = \frac{I*t_d}{m*\Delta V} \quad (4)$$

where I is the discharge current (A), t_d is the discharge time (s), m is the mass of the carbon material loaded on the working electrode (g), and ΔV is the potential window (1.1 V).

To quantify the charge storage behavior of the electrode explicitly, a power law was used as shown in Eq. 5:

$$i = av^b \quad (5)$$

where i (A g^{-1}) is the sum of surface-controlled (capacitive) and diffusion-controlled current contributions, a and b are adjustable parameters, and ν is the applied scan rate (mV s^{-1}). For values of $b \sim 1$, a surface-controlled charge storage mechanism prevails. For b values ~ 0.5, a diffusion-controlled energy storage process dominates.[34] The contributions from the surface-controlled (capacitive) and diffusion-controlled processes can be evaluated quantitatively using the following Eq. 6:[38-40]

$$i(V) = k_1 v + k_2 v^{1/2} \quad (6)$$

where i, v, k_1, and k_2 indicate the current, scan rate, and constants, respectively.

For symmetric supercapacitor cells, working electrodes were prepared by grinding a mixture of active material (PAM_4-HPC-K800), polyvinylidene fluoride and carbon black (weight percent, % 80 : 10 : 10) in ethanol. Solvent was added and the mixture was ground for about 30 minutes to obtain a homogenous slurry. The slurry was then spread on the carbon cloth substrate (1 cm × 1 cm) and air-dried at 80 °C overnight. The prepared electrodes had similar masses (1.1 mg each) and were immersed in 1 M H_2SO_4 electrolyte for further measurements. Cyclic voltammetry measurements (scanning rate of 5−100 mV s^{-1}) and galvanostatic charge-discharge tests (current density of 0.5−20 A g^{-1}) were performed using a BioLogic station VSP-3e (Grenoble, France). The specific capacitance (C_s, F g^{-1}) of the symmetric supercapacitor device was evaluated from the GCD curves using Eq. (4) multiplied by 2.

The energy density and power density of the symmetric supercapacitor were evaluated according to the following Eq. 7 and 8:

$$E = \frac{0.5 \cdot C_s \cdot (\Delta V^2)}{3.6} \quad (7)$$

$$P = \frac{3600 \cdot E}{t_d} \quad (8)$$

where E (Wh kg^{-1}) is energy density, and P (W kg^{-1}) is power density.[34]

RESULTS AND DISCUSSION

A semi-interpenetrated polymer network (SIPN) consisting of a polyacrylamide (PAM) network and hydroxypropyl cellulose (HPC) polymer was prepared using radical (co)polymerization. PAM acts as a carbon, oxygen, and nitrogen source, with HPC used as an additional source of carbon

and oxygen. Scheme 1 shows the synthesis method for PAM-HPC hydrogel-derived carbon materials activated by K_2CO_3 (for more details see the Experimental Section).

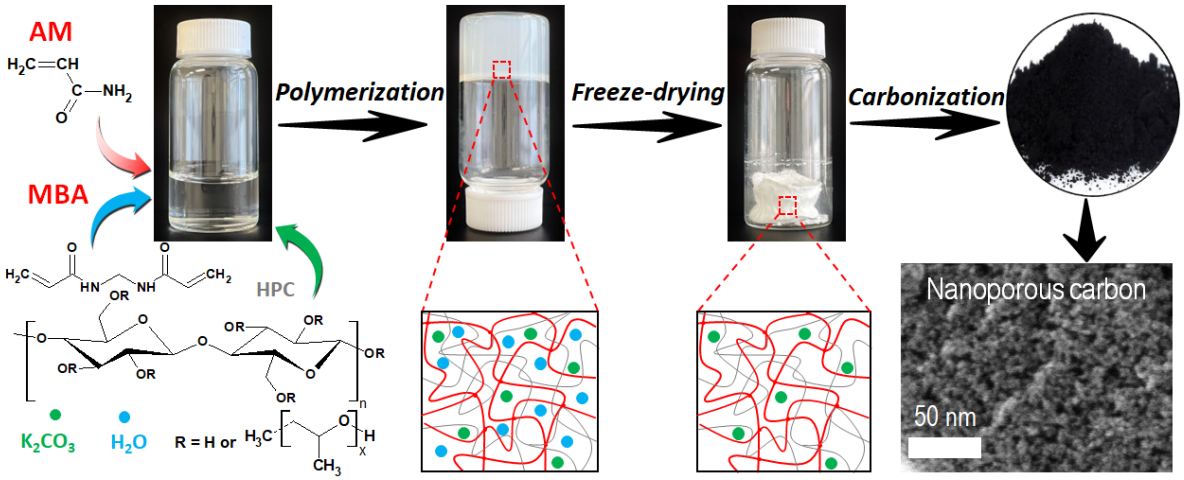

Scheme 1. Synthesis of K_2CO_3activated PAM-HPC hydrogel-derived carbon materials.

Figure 1a shows TGA profile of K_2CO_3 incorporated PAM_4-HPC hydrogel. Below 200 °C, weight loss is associated with the evaporation of trapped water from the hydrogel pores.[41]

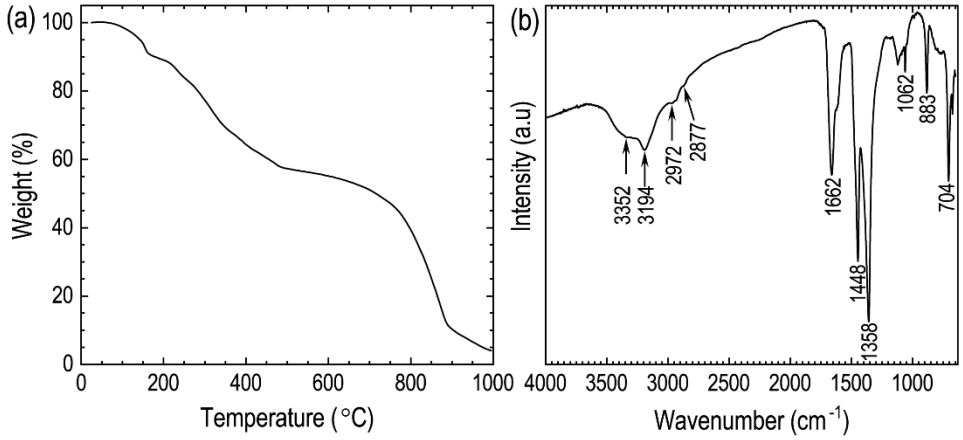

Figure 1. (a) TGA and (b) FTIR spectrum of PAM_4-HPC K_2CO_3 activated hydrogel.

Subsequently, in the temperature range of 200-500 °C, decomposition of the side amide groups, main PAM backbone, cellulose units and three-dimensional network occurs with a weight loss of about 30%.[41] Carbon material forms at temperatures above 500 °C, so that the following

carbonization temperatures were selected for study: 500, 700, 800, and 900 °C. Note that prepared hydrogel contains a fixed amount of potassium carbonate in its structure. Therefore, the melting temperature of K_2CO_3 (900 °C in N_2 atmosphere) should be considered. The thermal decomposition of K_2CO_3 releases volatile compounds (K_2O and CO_2) leading to weight loss in this temperature region.[42] As reported previously, substantial weight loss occurs during heating of potassium carbonate even below its melting point. Consequently, for PAM_4-HPC-K hydrogel, we can assume that drastic weight loss above 800 °C is influenced by the decomposition reactions of potassium carbonate (Eq.1, 2 and 3). Figure 1b shows FTIR spectrum of PAM_4-HPC hydrogel. FTIR bands at 3352 cm^{-1} and 3194 cm^{-1} correspond to N–H and O–H stretching vibrations from polyacrylamide and pyranose units of hydroxypropyl cellulose, respectively.[43] The bands at 2972 and 2877 cm^{-1} are assigned to CH_2 stretching vibrations and –N–CH_2– bonds from the crosslinking bridges.[43,44] Bands at 1662 and 1448 cm^{-1} are characteristic of the carbonyl group (C=O) stretching vibration and the C–N stretching, respectively.[43] After heat treatment, the intensity of FTIR peaks due to nitrogen- and oxygen-containing functionalities decreases substantially due to the high temperatures of carbonization (Figure S1).

Nitrogen adsorption/desorption isotherms were recorded to examine the surface textural properties of PAM-HPC-derived porous carbon materials (Figure 2). Directly carbonized reference sample, PAM_4-HPC-800 shows a low nitrogen uptake, which is represented by the Type-III isotherm indicating its nonporous nature. BET surface area is ca. 92.4 $m^2\ g^{-1}$.[23,45] The introduction of the activator, K_2CO_3 plays a significant role in developing the porosity of carbon materials. During the carbonization process, K_2CO_3 reacts with the carbon precursor (in this case, PAM-HPC), forming volatile gases (e.g. CO_2, H_2O), which exit the carbon framework.[18,19] These released gases cause the formation of pores within the carbon skeleton resulting in large specific

surface area and high nitrogen uptake. Increasing the annealing temperature from 500 to 800 °C leads to substantial increases in nitrogen uptake in the low relative pressure region ($P/P_0<0.1$) signifying the formation of a large number of micropores (Type I isotherm) (Figure 2a,b). However, increasing the temperature further to 900 °C (PAM_4-HPC-K900) causes micropore coalescence resulting in the formation of mesopores. The isotherm changes from Type-I to a mixed Type-I and Type-IV with a hysteresis loop in the middle-pressure region ($0.4 < P/P_0 < 0.6$: Figure 2a) due to the occurrence of capillary condensation.[23] This indicates that this carbon material has a hierarchically micro- and mesoporous structure. This is further supported by the pore-size distribution profiles obtained by using DFT method (Figure 2c) and BJH model (Figure 2d), which confirm the micro- and mesopore architecture of these carbon materials. The presence of the mesoporous structures in the microporous carbon is advantageous for supercapacitor applications as they promote the electrolyte ion diffusion towards the electrode surface.

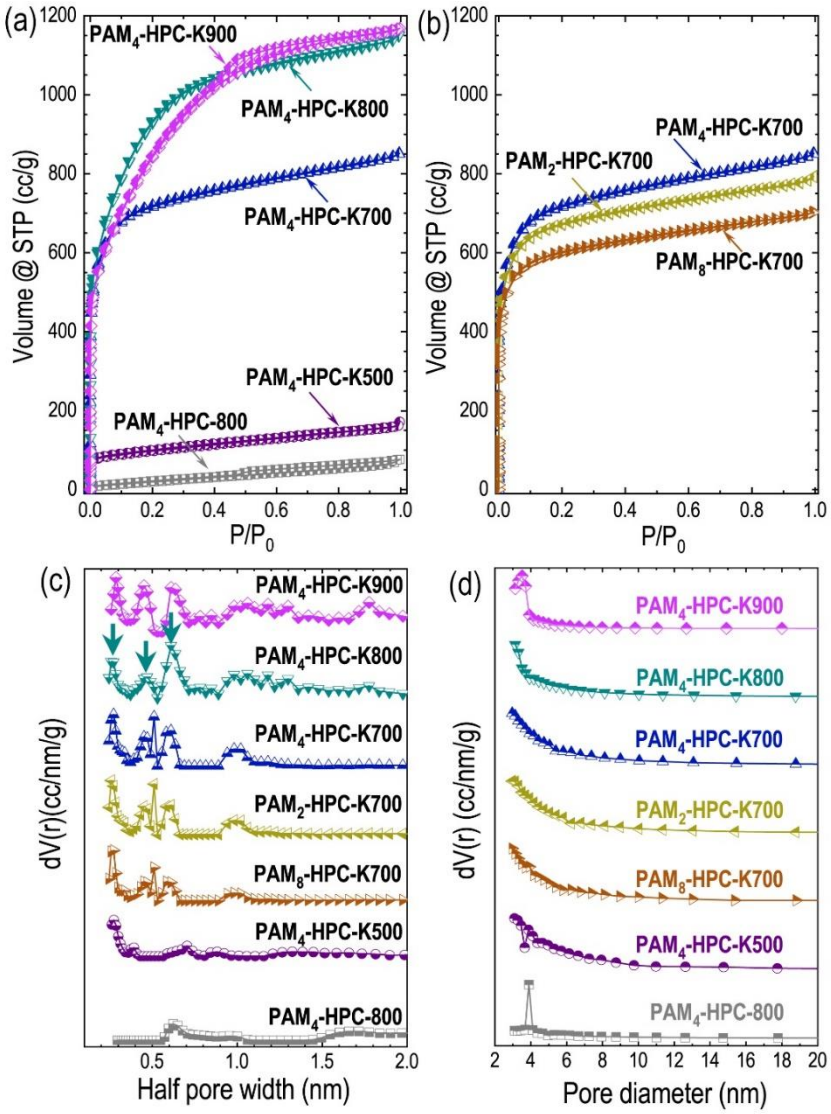

Figure 2. Surface textural properties obtained by nitrogen sorption measurements. (a) Nitrogen sorption isotherms of PAM_4-HPC-800, PAM_4-HPC-K500, PAM_4-HPC-K700, PAM_4-HPC-K800, PAM_4-HPC-K900 samples; (b) Nitrogen sorption isotherms of PAM_2-HPC-K700, PAM_4-HPC-K700, PAM_8-HPC-K700; (c) pore-size-distribution profiles from the DFT method; and (d) pore-size-distribution profiles obtained from the BJH model.

The sample carbonized at 800 °C (PAM_4-HPC-K800) exhibits optimal surface textural properties probably because at this temperature there exists a balance between the degradation of

the polymeric carbon network and the formation of 2D carbon. This is supported by the TGA analysis (Figure 1a), where a substantial weight loss is observed at about 800 °C assigned to the degradation of the carbon network. BET surface area and pore volume are ca. 3387.2 m^2 g^{-1} and 1.963 cm^3 g^{-1}, respectively. These values are much higher than the commercially available activated carbon materials or other porous carbon materials derived from other synthetic carbon sources including fullerene crystals.[46-49] K_2CO_3 also introduces defects or structural irregularities in the carbon lattice, which can function as active sites for electron transfer further improving the prospects of these materials in energy storage applications.

Compared to the effect of temperature, the PAM concentration in the hydrogel exerts only a minor influence on the surface area. This is most probably due to the balanced elemental composition and textural properties of the derived carbons. The PAM_4-HPC-K700 obtained from the hydrogel with 4 wt.% of PAM and cellulose shows the largest BET surface area (2712.6 m^2 g^{-1}) compared to the carbons prepared using 2 wt.% (2546.6 m^2 g^{-1}) and 8 wt.% (2295.3 m^2 g^{-1}) of PAM (Figure 2b). The textural properties of the prepared carbon materials are shown in Table 1. Note that as the temperature increases from 700 to 900 °C, mesopores' size and pore volume increase (Table 1), which benefits the electrolyte charge transport through the porous carbon network. As for the micropores, PAM4-HPC-K800 has the largest micropores, which are well-wetted by the electrolyte ions and allow their moderate diffusion onto the inner surface of the electrode carbon material.

Table 1. Surface area and porosity properties of nanoporous carbon materials obtained by the K_2CO_3 activation of PAM-HPC hydrogel[1].

Sample	S_{BET} (m^2 g^{-1})	S_{micro} (m^2 g^{-1})	V_p (cm^3 g^{-1})	V_{micro} (cm^3 g^{-1})	V_{meso} (cm^3 g^{-1})	W_p (nm)	D_p (nm)

PAM_4-HPC-800	92.4	61.3	0.215	0.109	0.106	----	3.89
PAM_4-HPC-K500	349.5	424.2	0.353	0.231	0.122	0.274	3.09
PAM_4-HPC-K700	2712.6	2681.2	1.485	1.254	0.231	0.273	2.97
PAM_4-HPC-K800	3387.2	2919.6	1.963	1.694	0.269	0.610	3.13
PAM_4-HPC-K900	3081.9	2698.7	2.187	1.733	0.454	0.286	3.51
PAM_2-HPC-K700	2546.6	2565.2	1.374	1.166	0.208	0.259	2.97
PAM_8-HPC-K700	2295.3	2405.5	1.217	1.041	0.176	0.273	2.97

[1] S_{BET} = BET surface area, S_{micro} = micropore surface area, V_p = pore volume (total), V_{micro} = pore volume from micropores, V_{meso} = pore volume from mesopores, W_p = average half pore width, D_p = average mesopore diameter.

Figure 3 shows SEM images of the K_2CO_3 activated carbon materials. SEM images of the hydrogel (PAM_4-HPC) and additional SEM images of the prepared carbon materials are provided in the Supplementary Information (Figure S2: PAM_4-HPC, Figure S3: PAM_4-HPC-K500, Figure S4: PAM_4-HPC-K700, Figure S5: PAM_4-HPC-K800, Figure S6: PAM_4-HPC-K900, Figure S7: PAM_2-HPC-K700, and Figure S8: PAM_8-HPC-K700). At the macroscale, morphology of the carbonized samples has a honeycomb-like irregular structure (Figure 3a,c,e,g,i,k). High-resolution SEM images reveal that the mesoporosity of the PAM_4-HPC-derived carbons seems to increase with increasing carbonization temperature reaching a maximum at 800 °C (Figure 3b,d,f,g and Figure S3-6). The PAM_2-HPC-K700 and PAM_8-HPC-K700 samples have similar internal pore structures (Figure 3j and Figure 3l). TEM images (Figure 4a,b) further confirm the presence of well-developed mesoporous structures. Microporous amorphous carbon structures can be observed in HR-TEM images (Figure 4c,d) indicating the hierarchically porous motif of the prepared carbon material.

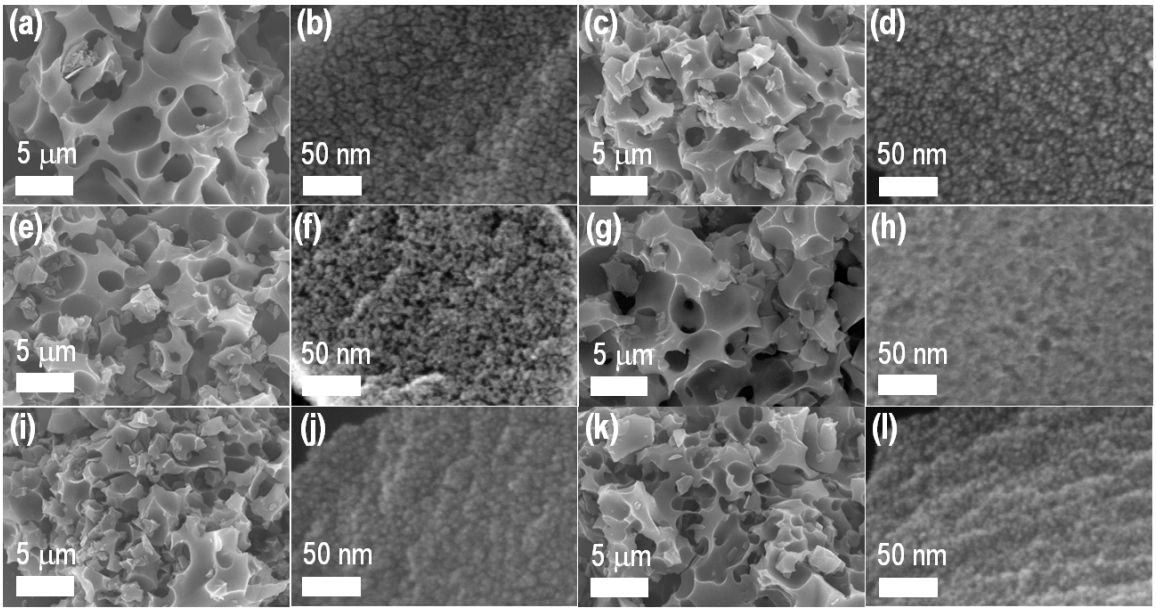

Figure 3. SEM images of PAM_4-HPC-derived carbon materials. (a, b) PAM_4-HPC-K500; (c, d) PAM_4-HPC-K700; (e, f) PAM_4-HPC-K800; (g, h) PAM_4-HPC-K900; (i, j) PAM_2-HPC-K700; and (k, l) PAM_8-HPC-K700.

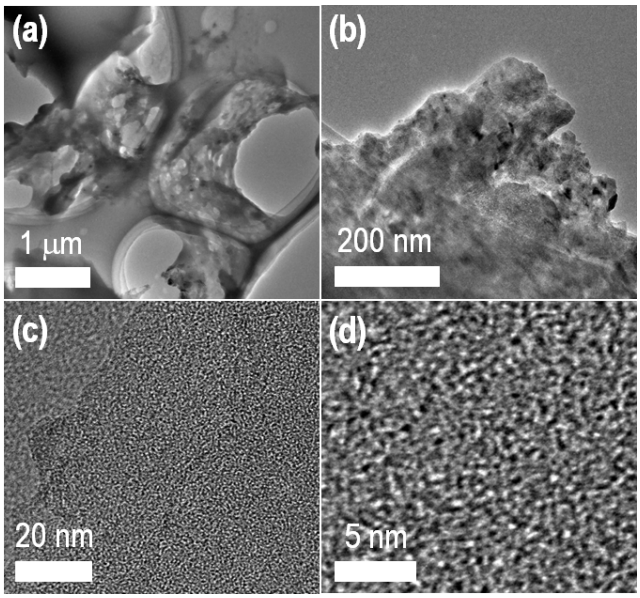

Figure 4. (a, b) TEM images of PAM_4-HPC-K800, and (c, d) the corresponding HR-TEM images.

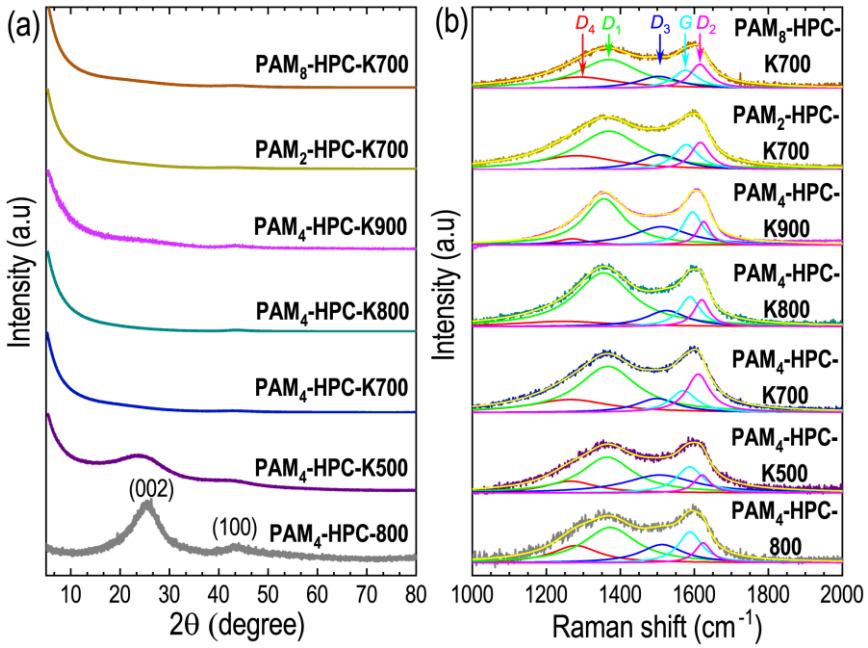

Figure 5. (a) XRD patterns and (b) Raman scattering spectra of PAM_4-HPC-800 reference sample and the activated carbon samples with the deconvoluted curves: PAM_4-HPC-K500, PAM_4-HPC-K700, PAM_4-HPC-K800, PAM_4-HPC-K900, PAM_2-HPC-K700, and PAM_8-HPC-K700.

Figure 5a shows XRD patterns of directly carbonized PAM-HPC and the K_2CO_3-activated carbon materials. The patterns contain two broad diffraction peaks at 2θ = 25.4° and 43.6°, corresponding to the (002) and (100) planes of disordered graphite-like structures of amorphous carbon, respectively. The (002) peak is the most intense in the XRD pattern of graphite, and it is sensitive to the stacking order of the carbon layers. The (100) peak is less intense than the (002) peak and is less sensitive to the stacking order of the carbon layers. K_2CO_3 activation contributes to the formation of a larger number of pores and defect sites in the carbon lattice. This is indicated by a reduced intensity of the (002) peak. The (002) peak is attenuated because pores and defects disrupt the stacking order of the carbon layers. Increasing the carbonization temperature above 700 °C leads to strong attenuation of the (002) peak, which is the result of the formation of randomly

oriented highly porous carbon materials. The persistence of the (100) peak in all the samples suggests that the carbon layers remain stacked in a relatively ordered fashion.[26,27] Overall, the XRD results indicate that K_2CO_3 activation promotes the formation of pores and defect sites in the carbon materials.

Raman scattering spectra (Figure 5b) contain two peaks located at ~1360 cm^{-1} and 1600 cm^{-1} corresponding respectively to *D* (disordered structure) and *G* (graphitic structure) bands of carbon materials.[50] In order to gain more information about the intrinsic features of these carbon materials, the fitting of Raman spectra using Lorentzian-shaped bands was performed.[51-53] The fitting includes an ideal graphitic *G*-band at about ~1580 cm^{-1} and disordered graphitic lattice *D*-bands, namely, D_1, D_2, D_3, D_4. More specifically, D_1 (~1360 cm^{-1}) is due to graphene layer edges, D_2 (~1620 cm^{-1}) the surfaces of graphitic layers, D_3 (~1510 cm^{-1}) amorphous carbon and heteroatom-doped carbon, and D_4 (~1270 cm^{-1}) is due to polyenes and ionic impurities, e.g. potassium cations.

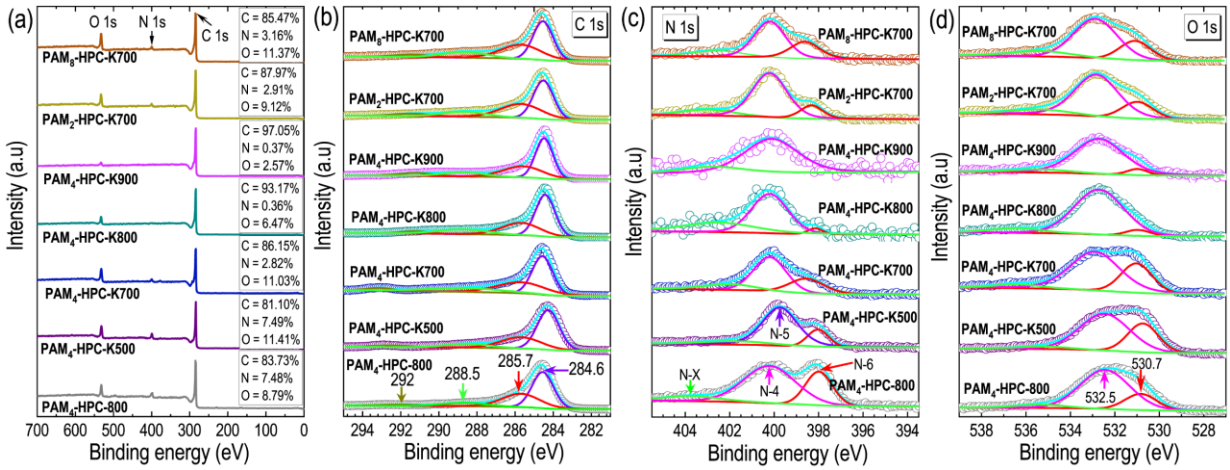

Figure 6. XPS spectra of PAM-HPC hydrogel-derived carbons. (a) XPS survey spectra of PAM_4-HPC-800, PAM_4-HPC-K500, PAM_4-HPC-K700, PAM_4-HPC-K800, PAM_4-HPC-K900, PAM_2-HPC-K700, PAM_8-HPC-K700; (b) XPS C 1s core level spectra with the deconvoluted peaks; (c) XPS N 1s core level spectra with the deconvoluted peaks; (d) XPS O 1s core level spectra with the deconvoluted peaks.

Surface compositions and chemical states of the elements in PAM-HPC hydrogel-derived carbon materials were studied using XPS (Figure 6). Survey spectra of the carbon materials reveal three main peaks at ~ 284, 400, and 532 eV, which correspond to C 1s, O 1s, and N 1s components, respectively (Figure 6a). Increasing the carbonization temperature leads to decreases in nitrogen and oxygen contents, indicated by the lower intensities of O 1s, and N 1s peaks in XPS spectra. The C 1s spectra of PAM-HPC hydrogel-derived carbon materials were deconvoluted into four peaks, with those centered at 284.6, 285.7, 288.5, and 292.0 eV corresponding to C=C (sp^2), C–N/C–C (sp^3), C=O and O-C=O bonding states, respectively (Figure 6b). Deconvolution of N 1s spectra revealed three types of nitrogen at the surfaces of carbon samples (Figure 6c). The signal at ~398.0 eV is assigned to pyridinic nitrogen (N-6), that at ~400.2 eV is due to graphitic N (N-4), and the peak at ~403.7 eV is attributed to N-oxide (N-X).[54-56] For PAM_4-HPC-K500, some pyrrolic (N-5) nitrogen indicated by the peak at 399.8 eV could also be observed. Further increasing the temperature of carbonization leads to the emergence of graphitic nitrogen (N-4) as the prevalent form, which contributes positively to the electrical conductivity of the supercapacitor electrode. However, since nitrogen content in these carbon materials is significantly decreased above 800 ℃, we consider that the micro/mesoporous architectures and the overall surface textural properties play the most significant role in the performance of supercapacitor electrodes. O 1s XPS spectra were deconvoluted to peaks at 530.7 eV, 532.5 eV, and 535.4 eV, which correspond to C=O, C–O–C, and O−C=O groups, respectively, with carbonyl and ester groups being most abundant (Figure 6d). Overall, the presence of graphitic nitrogen in the carbon structure improves electrical conductivity, whereas pyridinic, and pyrrolic nitrogen as well as oxygen functionalities promote redox reactions and wettability of the carbon surface, which is beneficial for high-performance supercapacitors.

Inspired by the favorable characteristics for energy storage applications, including ultrahigh surface area, well-developed hierarchically porous architecture, large pore volume, intrinsic nitrogen and oxygen dopants of the PAM-HPC hydrogel-derived carbons, the electrochemical supercapacitance performance was studied by CV, GCD, and EIS measurements in aqueous electrolyte (1 M H_2SO_4). Figure 7a compares the CV curves of selected samples at a fixed scan rate of 50 mV s^{-1} in the potential window of 1.1 V (from -0.1−1V).

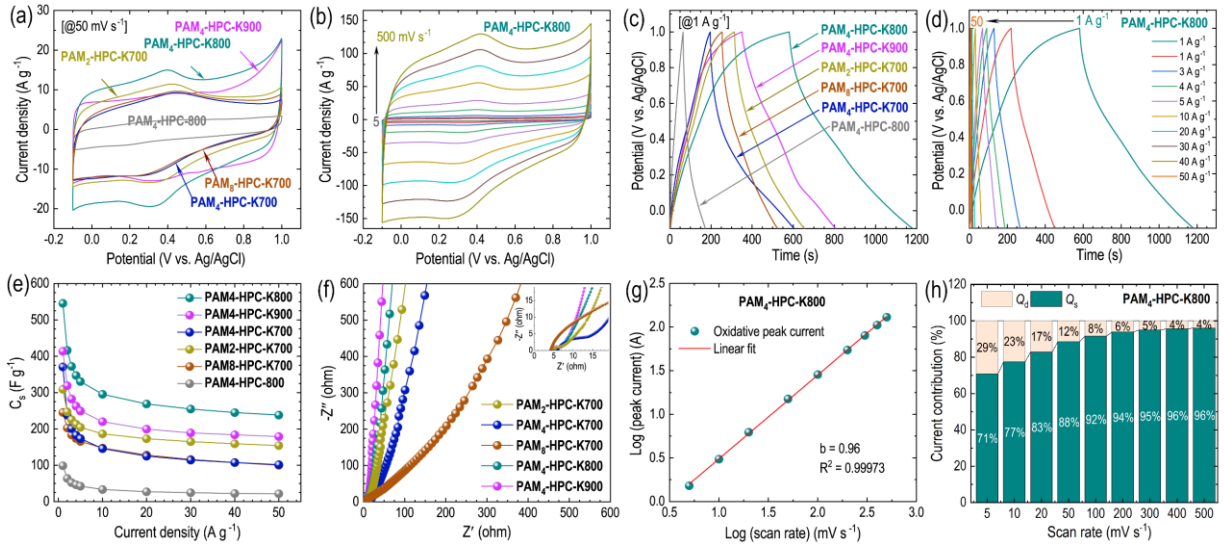

Figure 7. (a) Comparison of the CV profiles of PAM-HPC carbon materials at 50 mV s^{-1}; (b) CV profile of PAM_4-HPC-K800 at different scan rates (5−500 mV s^{-1}); (c) comparison of the GCD profiles of the prepared carbon materials at current density of 1 A g^{-1}; (d) GCD profiles at different current densities (1 to 50 A g^{-1}) for a sample with optimal surface area (PAM_4-HPC-K800); (e) calculated specific capacitance C_s vs. current density and (f) Nyquist plots for PAM_2-HPC-K700, PAM_4-HPC-K700, PAM_8-HPC-K700, PAM_4-HPC-K800, PAM_4-HPC-K900; (g) logarithm relationship of oxidation peak current versus scan rate; (h) Capacitive or Surface-controlled (Q_s) and diffusion-controlled (Q_d) current contribution of the PAM_4-HPC-K800 electrode analyzed at various scan rates.

The CV profiles have a quasi-rectangular shape, which is important for the EDLC-type energy storage mechanism (Figure 7a).[57] Weak redox peaks obtained in the CV profiles at 0.3 and 0.4 V can be attributed to the presence of the nitrogen and oxygen dopants. Figure 7b shows the CV profiles at different sweep rates. At a faster potential sweep (500 mV s^{-1}), the quasi-rectangular shape of CV profiles is maintained, indicating rapid diffusion of H^+ ions to the electrode surface promoted by the hierarchical porosity and appropriate pore size of the materials. GCD profiles of directly carbonized PAM_4-HPC-800 and K_2CO_3-activated samples measured at a current density of 1 A g^{-1} are shown in Figure 7c. All the GCD curves have a quasi-triangular shape typical of an electrical double-layer capacitor (EDLC).[58-62] GCD curves indicate that PAM_4-HPC-K800 has the longest discharge time, which is consistent with it having the largest surface area of the materials studied, and also indicates the largest energy storage capacitance. Figure 7d shows the GCD curves for PAM_4-HPC-K800 measured at different current densities (1−50 A g^{-1}). GCD curves retain a quasi-triangular shape even at higher current densities (Figure S9), which can be attributed to the rapid transfer of electrolyte ions to the surface of the carbon electrode. Specific capacitances C_s calculated from GCD curves using Eq. 4 are represented in Figure 7e. The optimal sample achieved the highest specific capacitance ca. 545.5 F g^{-1} at a current density of 1 A g^{-1} with 43.7% capacitance retention at a high current density of 50 A g^{-1} (Figure S10a) and an outstanding cycle life of 96.3% after 5000 charging-discharging cycles (Figure S10b). Such a high value of the specific capacitance and a good rate performance can be attributed to the synergy effect of ultrahigh surface area caused due to the abundant micro- and mesopores, and nitrogen doping. C_s values of other samples are ca. 413.6 F g^{-1} (PAM_4-HPC-K900), 370.1 F g^{-1} (PAM_4-HPC-K700), 309.1 F g^{-1} (PAM_2-HPC-K700), 245.5 F g^{-1} (PAM_8-HPC-K700), and 98.7 F g^{-1} (PAM_4-HPC-800). Pore size and distribution affect electrode performance. As preparation temperature increases from

700 to 900 °C, the dimensions and pore volume of mesopores increases, having a beneficial impact on electrolyte ion transport through the porous carbon network. Regarding the micropores, PAM_4-HPC-K800 has large micropores which are well-wetted by the electrolyte ions and allow their moderate diffusion onto the inner surface of the electrode carbon material. Nyquist plots acquired by EIS measurements provide information on the charge storage mechanism of the prepared capacitive materials (Figure 7f). A vertical line in the low-frequency region is characteristic of EDLC materials, whereas the presence of the weak semicircular response in the high-frequency region is caused by the presence of N and O functional groups on the surface of the electrode material.[17] The values of equivalent series resistance (ESR)[23,63] obtained from the intersection point between the real and imaginary axes are as follows: 4.85 Ω (PAM_2-HPC-K700), 5.96 Ω (PAM_4-HPC-K700), 4.30 Ω (PAM_8-HPC-K700), 4.67 Ω (PAM_4-HPC-K800), 4.17 Ω (PAM_4-HPC-K900), which indicate the good electrical conductivity of PAM-HPC hydrogel-derived carbon materials. Furthermore, the contribution of each charge storage mechanism was evaluated using the classification of capacitive or surface-controlled to diffusion-controlled energy storage contributions.[64,65] Since the b value obtained using Eq. 5 is 0.96 (Figure 7g), the surface-controlled charge storage mechanism prevails over the diffusion-controlled contribution and its dominance increases at higher scan rates (Eq. 6, Figure 7h).[66] Based on the electrochemical experiments, PAM_4-HPC-K800 has an extremely high C_s value, rather low internal resistance, and excellent capacitance performance. For these reasons, it was used in further measurements incorporated in a symmetrical cell device.

A schematic illustration of a symmetric supercapacitor device is shown in Figure 8a. Figure 8b shows the CV response of the device at different scan rates from 5 to 100 mV s^{-1} in the potential window of 1.1 V. These data indicate the capacitive behavior typical of an electrical double-layer

supercapacitor.[67] With increasing scan rate, the CV profiles diverge from the ideal rectangular shape due to charge transport resistance. GCD profiles of the device recorded at different current densities (0.5 – 20 A g^{-1}) are shown in Figure 8c. The charge-discharge curves have a nearly symmetrical triangular shape from low to high current densities (Figure 8c and Figure S11), indicating EDLC behavior with well-balanced charge storage. The gravimetric specific capacitance of the cell calculated from GCD data is 102.5 F g^{-1} at 0.5 A g^{-1} (Figure 8d). Moreover, the supercapacitor cell has a low resistance, indicated by the absence of a voltage (IR) drop. Figure 8e shows Nyquist plots of the device obtained by EIS measurements performed prior to and following stability measurements. The semi-circular behavior in the high frequency region with approximately 45° slope in the low frequency region in the EIS curves infers charge transfer resistance and Warburg impedance that are often present for carbon materials containing nitrogen and oxygen. EIS data were fitted using an equivalent circuit (Inset of Figure 8e). From the fitting, solution (R_s) and charge transfer resistance (R_{ct}) of the device before and after cycle tests were ca. 0.512 Ω and 0.101 Ω, and 0.524 Ω and 0.091 Ω, respectively. Long-term cycling durability tests of the supercapacitor cell were performed at a current density of 10 A g^{-1} during 5000 cycles (Figure 8f). The material exhibits an outstanding cycling stability with 94.2% capacitance retention and 99.3% coulombic efficiency after 5000 consecutive charge-discharge cycles (Figure 8f).

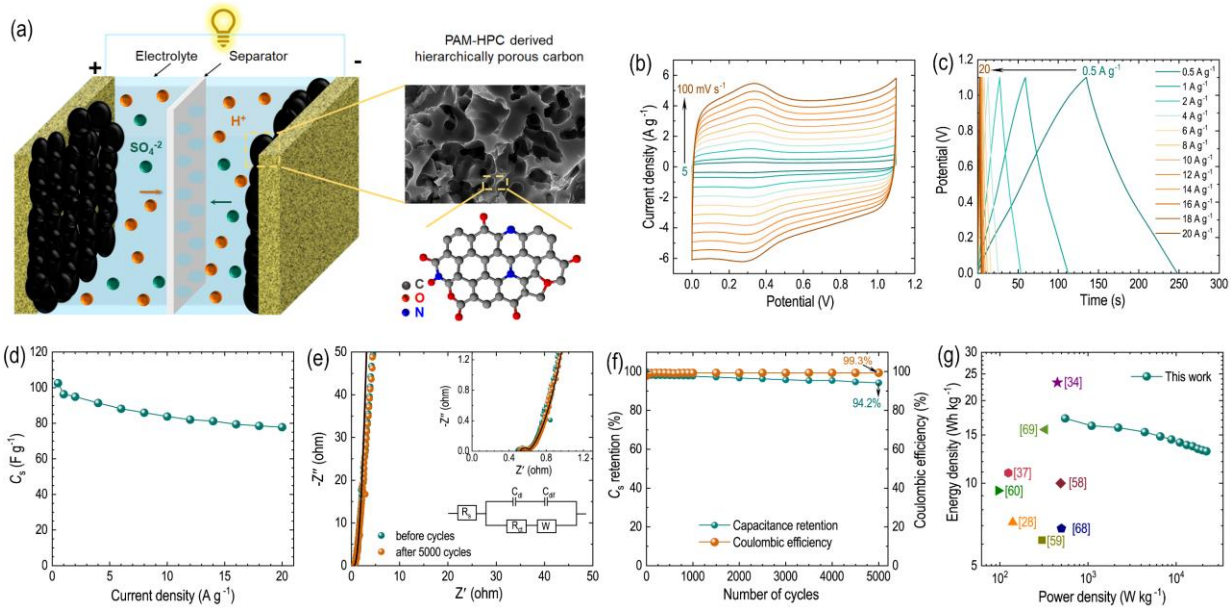

Figure 8. (a) Schematic illustration of a symmetric supercapacitor device based on PAM-HPC carbon. (b) CV curves of PAM_4-HPC-K800 supercapacitor device at different scan rates from 5 to 100 mV s^{-1}. (c) GCD curves at different current densities from 0.5 to 20 A g^{-1} in the voltage range of 0−1.1 V. (d) calculated specific capacitance C_s vs. current density. (e) Nyquist plots of the supercapacitor before and after cycling measurements. (f) Capacitance retention at a current density of 10 A g^{-1} and coulombic efficiency. (g) Ragone plot. The inset of panel (e) represents the equivalent circuit diagram, where R_s, R_{ct} represents the solution and charge transfer resistance. C_{dl}, C_{dif}, and W represents the double layer formation, diffusion contribution, and Warburg diffusion resistance.

The energy performance of the assembled symmetric supercapacitor device is shown in the Ragone plot (Figure 8g). The device achieved a high energy density of 17.2 Wh kg^{-1} (Eq. 7) at a power density of 550 W kg^{-1} (Eq. 8), which is superior to/or comparable to the performance of previously reported porous carbon materials, such as $ZnCl_2$-$CaCl_2$ molten salt-activated chitin carbon,[28] PAM hydrogel activated carbon,[34] PAM-glucose hydrogel KOH activated carbon,[37]

Tasmanian blue gum tree bark derived carbon,[58] carbon nitride derived from melamine and citric acid, and activated using KOH,[59] KOH activated pomelo peel derived carbon,[60] $K_2B_4O_7$ and K_2CO_3 carboxymethyl chitosan hydrogel-derived carbon,[68] and quantum dots/reduced graphene oxide composite derived carbon.[69] The electrochemical results demonstrate that K_2CO_3-activated PAM-HPC hydrogel porous carbons exhibit hierarchically micro-mesoporous structures, ultrahigh surface area, and self-heteroatom doping. Therefore, they are promising supercapacitor electrode materials offering high energy density, excellent rate performance and cycle life.

CONCLUSIONS

To conclude, hierarchically porous carbons with ultrahigh surface area and well-defined pore structures were prepared by K_2CO_3 activation of polyacrylamide-cellulose (PAM-HPC) hydrogel at different carbonization temperatures (500−900 °C). The presence/absence of the activation agent and carbonization temperature are the factors that influence most significantly the pore-size modulation/formation. Carbonization at 800 °C yielded nanoporous carbon material with an ultrahigh surface area of 3387.2 $m^2\ g^{-1}$ and a large pore volume of 1.963 $cm^3\ g^{-1}$. The electrode prepared using this material demonstrated excellent supercapacitance performance, giving a high specific capacitance of 545.5 F g^{-1} at 1 A g^{-1} in the three-electrode cell setup together with high rate performance and long cycle life of 96.3% after 5000 charging-discharging cycles. Additionally, the optimal sample was used to assemble a symmetric supercapacitor device operable in the potential window of 1.1 V in an aqueous electrolyte (1M KOH). The device achieved a specific capacitance of 102.5 F g^{-1} at 0.5 A g^{-1}. It gave a high energy density of 17.2 Wh kg^{-1} at the power density of 550 W kg^{-1} with an excellent cycle life of 94.2% after 5000 charging-discharging cycles, demonstrating that activated polyacrylamide-cellulose (PAM-HPC)

hydrogel-derived nanoporous carbon materials have enormous potential in high-performance supercapacitor applications.

ASSOCIATED CONTENT

Supporting Information. The Supporting Information is available free of charge on the ACS Publications website at DOI: XX.XXXX/XXX.XXX. FTIR spectra of PAM_4-HPC-K500, PAM_4-HPC-K700, PAM_4-HPC-K800, PAM_4-HPC-K900, PAM_2-HPC-K700, PAM_8-HPC-K700. SEM images of PAM_4-HPC hydrogel, and additional SEM images of PAM_4-HPC-K500, PAM_4-HPC-K700, PAM_4-HPC-K800, PAM_4-HPC-K900, PAM_2-HPC-K700, and PAM_8-HPC-K700. GCD profiles of PAM4-HPC-K800 electrode at higher current densities (10 – 50 A g^{-1}), capacitance retention (C_s) of the prepared carbon electrodes at a high current density of 50 A g^{-1}, cycling stability of PAM_4-HPC-K800 electrode at 50 A g^{-1}, and GCD profiles of the symmetric cell at higher current densities (6 – 20 A g^{-1}), and a comparison table of the electrochemical supercapacitance performance of the optimal sample, PAM_4-HPC-K800 with other carbon materials derived from different carbon sources.

AUTHOR INFORMATION

Corresponding Authors

Nadiia Velychkivska (Email: velychkivska.nadiia@nims.go.jp)

Jonathan P. Hill (Email: jonathan.hill@nims.go.jp)

Jan Labuta (Email: LABUTA.Jan@nims.go.jp)

Lok Kumar Shrestha (Email: SHRESTHA.Lokkumar@nims.go.jp)

Author Contributions

Conceptualization, N.V., L.K.S.; methodology, N.V., L.K.S., A.P., A.G.; investigation, N.V., L.K.S., R.M., P.A.S., A.P.; data curation, N.V., L.K.S., A.P., R.M., and P.A.S.; writing—original draft preparation, N.V. and L.K.S.; writing—review and editing, N.V., L.K.S., J.L., Y.Y., and J.P.H.; supervision, L.K.S.; project administration, L.K.S.; funding acquisition, N.V., K.A., Y.Y., and J.P.H. All authors have read and agreed to the published version of the manuscript.

Notes

The authors declare no competing financial interest.

ACKNOWLEDGMENT

N.V. is grateful for financial support from the Japan Society for the Promotion of Science (JSPS) for a JSPS postdoctoral fellowship (P21764) supported by JSPS KAKENHI Grant Number JP22KF0385. The authors are grateful to JST-ERATO Yamauchi Materials Space-Tectonics Project (JPMJER2003) and the Queensland Node of the Australian National Fabrication Facility (ANFF-Q). This work is also partially supported by JSPS KAKENHI Grant Number JP20H00392 and JP23H05459.

REFERENCES

1. Lokhande, P. E.; Chavan, U. S.; Pandey, A. Materials and fabrication methods for electrochemical supercapacitors: overview. *Electrochem. Energ. Rev.* **2020**, *3*, 155–186, https://doi.org/10.1007/s41918-019-00057-z.

2. Shrestha, R. G.; Maji, S.; Shrestha, L. K. Nanoarchitectonics of nanoporous carbon materials in supercapacitors applications. *Nanomaterials* **2020**, *10*, 1–27, https://doi.org/10.3390/nano10040639.
3. Zhao, J.; Burke, A. Review on supercapacitors: technologies and performance evaluation. *J. Energy Chem.* **2020***, 59*, 276-291, https://doi.org/10.1016/j.jechem.2020.11.013.
4. Muzaffar, A.; Ahamed, M. B.; Deshmukh, K.; Thirumalai, J. A review on recent advances in hybrid supercapacitors: design, fabrication and applications. *Renew. Sustain. Energy Rev.* **2019**, *101*, 123–145, https://doi.org/10.1016/j.rser.2018.10.026.
5. Najib, S.; Erdem, E. Current progress achieved in novel materials for supercapacitor electrodes: Mini Review. *Nanoscale Adv.* **2019**, *1*, 2817–2827, https://doi.org/10.1039/C9NA00345B.
6. Pershaanaa, M.; Bashir, S.; Ramesh, S.; Ramesh, K. Every bite of supercap: a brief review on construction and enhancement of supercapacitor. *J. Energy Storage* **2022**, *50*, 104599, https://doi.org/10.1016/j.est.2022.104599.
7. Dou, Q.; Park, H. S. Perspective on high-energy carbon-based supercapacitors. *Energy Environ. Mater.* **2020**, *3*, 286–305, https://doi.org/10.1002/eem2.12102.
8. Shi, F.; Li, L.; Wang, X.; Gu, C.; Tu, J. Metal oxide/hydroxide-based materials for supercapacitors. *RSC Adv.* **2014**, *4*, 41910–41921, https://doi.org/10.1039/C4RA06136E.
9. You, X.; Misra, M.; Gregori, S.; Mohanty, A. K. Preparation of an electric double layer capacitor (EDLC) using miscanthus-derived biocarbon. *ACS Sustainable Chem. Eng.* **2018**, *6*, 318–324, https://doi.org/10.1021/acssuschemeng.7b02563.
10. Dubey, P.; Maheshwari, P. H.; Priyanka, H.; Mansi, V.; Shrivastav, V.; Sundriyal, S. Effect of nitrogen and sulphur co-doping on the surface and diffusion characteristics of date seed-

derived porous carbon for asymmetric supercapacitors. *J. Energy Storage*, **2023**, *58*, 106441, https://doi.org/10.1016/j.est.2022.106441.

11. Silva, T. D.; Damery, C.; Alkhaldi, R.; Karunanithy, R.; Gallaba, D. H.; Patil, P. D.; Wasala, M.; Sivakumar, P.; Migone, A.; Talapatra S. Carbon nanotube based robust and flexible solid-state supercapacitor. *ACS Appl. Mater. Interfaces* **2021**, *13*, 56004-56013, https://doi.org/.1021/acsami.1c12551.
12. Pal, B.; Sarkar, K. J.; Wu, B.; Dekanovsky, L.; Mazánek, V.; Jose, R.; Sofer, Z. Exploration of charge storage behavior of binder-free EDL capacitors in aqueous electrolytes. *ACS Omega* **2023**, *8*, 2629–2638, https://doi.org/10.1021/acsomega.2c07143.
13. Boota, M.; Hatzell, K. B.; Alhabeb, M.; Kumbur, E. C.; Gogotsi, Y. Graphene-containing flowable electrodes for capacitive energy storage; *Carbon* **2015**, *92*, 142-149, https://doi.org/10.1016/j.carbon.2015.04.020.
14. Wong, S. I.; Lin, H.; Sunarso, J.; Wong, B. T.; Jia, B. H. Optimization of ionic-liquid based electrolyte concentration for high-energy density graphene supercapacitors. *Appl. Mater. Today* **2020**, *18*, 100522, https://doi.org/10.1016/j.apmt.2019.100522.
15. Gao, P.-C.; Tsai, W.-Y.; Daffos, B.; Taberna, P.-L.; Pérez, C. R.; Gogotsi, Y.; Simon, P.; Favier, F. Graphene-like carbide derived carbon for high-power supercapacitors. *Nano energy* **2015**, *12*, 197-206, https://doi.org/10.1016/j.nanoen.2014.12.017
16. Li, Z.; Guo, D.; Liu, Y.; Wang, H.; Wang, L. Recent advances and challenges in biomass-derived porous carbon nanomaterials for supercapacitors. *Chem. Eng. J.* **2020**, *397*, 125418, https://doi.org/10.1016/j.cej.2020.125418.
17. Maji, S.; Chaudhary, R.; Shrestha, R. G.; Shrestha, R. L.; Demir, B.; Searles, D. J.; Hill, J. P.; Yamauchi, Y.; Ariga, K.; Shrestha L. K. High-performance supercapacitor materials

based on hierarchically porous carbons derived from artocarpus heterophyllus seed. *ACS Appl. Energy Mater.* **2021**, *4*, 12257–12266, https://doi.org/10.1021/acsaem.1c02051.

18. Zhang, F.; Liu, T.; Hou, G.; Kou, T.; Yue, L.; Guan, R.; Li, Y. Hierarchically porous carbon foams for electric double layer capacitors. *Nano Res.* **2016**, *1*, 1–14, https://doi.org/10.1007/s12274-016-1173-z.

19. Dai, J.; Wang, L.; Xie, A.; He, J.; Yan, Y. Reactive template and confined self-activation strategy: three-dimensional interconnected hierarchically porous N/O-doped carbon foam for enhanced supercapacitors. *ACS Sustain. Chem. Eng.* **2020**, *8*, 739−748, https://doi.org/10.1021/acssuschemeng.9b01394.

20. Guo, Y.; Bae, J.; Fang, Z.; Li, P.; Zhao, F.; Yu, G. Hydrogels and hydrogel-derived materials for energy and water sustainability. *Chem Rev.* **2020**, *120*, 7642−7707, https://doi.org/10.1021/acs.chemrev.0c00345.

21. Zu, G.; Shen, J.; Zou, L.; Wang, F.; Wang, X.; Zhang, Y.; Yao, X. Nanocellulose-derived highly porous carbon aerogels for supercapacitors. *Carbon* **2016**, *99*, 203–211, https://doi.org/10.1016/j.carbon.2015.11.079.

22. Yu, M.; Li, J.; Wang, L. KOH-activated carbon aerogels derived from sodium carboxymethyl cellulose for high-performance supercapacitors and dye adsorption. *Chem. Eng. J.* **2017**, *310*, 300–306, https://doi.org/10.1016/j.cej.2016.10.121.

23. Shrestha, L. K.; Shrestha, R. G.; Chaudhary, R.; Pradhananga, R. R.; Tamrakar, B. M.; Shrestha, T.; Maji, S.; Shrestha, R. L.; Ariga, K. Nelumbo nucifera seed–derived nitrogen-doped hierarchically porous carbons as electrode materials for high-performance supercapacitors. *Nanomaterials* **2021**, *11*, 1–16, https://doi.org/10.3390/nano11123175.

24. Jin, Y.; Tian, K.; Wei, L.; Zhang, X.; Guo, X. Hierarchical porous microspheres of activated carbon with a high surface area from spores for electrochemical double-layer capacitors. *J. Mater. Chem. A* **2016**, *4*, 15968–15979, https://doi.org/10.1039/C6TA05872H.

25. Hou, J.; Cao, C.; Idrees, F.; Ma, X. Hierarchical porous nitrogen-doped carbon nanosheets derived from silk for ultrahigh-capacity battery anodes and supercapacitors. *ACS Nano* **2015**, *9*, 2556–2564, https://doi.org/10.1021/nn506394r.

26. Inagaki, M.; Toyoda, M.; Soneda, Y.; Morishita, T. Nitrogen-doped carbon materials. *Carbon* **2018**, *132*, 104–140, https://doi.org/10.1016/j.carbon.2018.02.024.

27. Basha, D. B.; Ahmed, S.; Ahmed, A.; Gondal, M. A. Recent advances on nitrogen doped porous carbon micro-supercapacitors: new directions for wearable electronics. *J. Energy Storage* **2023**, *60*, 106581, https://doi.org/10.1016/j.est.2022.106581.

28. Yang, P.; Zheng, D.; Zhu, P.; Jiang, F.; Bi, X. Biocarbon with large specific surface area and tunable pore structure from binary molten salt templating for supercapacitor applications. *Chem. Eng. J.* **2023**, *472*, 144785, https://doi.org/10.1016/j.cej.2023.144785.

29. Zhang, J.; Wu, D.; Zhang, Q.; Zhang, A.; Sun, J.; Hou, L.; Yuan, C. Green self-activation engineering of metal–organic framework derived hollow nitrogen-doped carbon spheres towards supercapacitors. *J. Mater. Chem. A* **2022**, *10*, 2932–2944, https://doi.org/10.1039/d1ta10356c.

30. Zhou, L.; Cao, H.; Zhu, S.; Houa, L.; Yuan, C. Hierarchical micro-/mesoporous N- and O-enriched carbon derived from disposable cashmere: a competitive cost-effective material for high-performance electrochemical capacitors. *Green Chem.* **2015**, *17*, 2373–2382, https://doi.org/10.1039/c4gc02032d.

31. Yang, Y.; Ma, Y.; Lu, C.; Li, S.; Zhu, M. Molten salt technique for the synthesis of carbon-based materials for supercapacitors. *Green Chem.* **2023**, *25*, 10209–10234, https://doi.org/10.1039/d3gc03525e.

32. Zhu, M.; Yang, Y.; Ma, Y. Salt-assisted synthesis of advanced carbon-based materials for energy-related applications. *Green Chem.* **2023**, *25*, 10263–10303, https://doi.org/ 10.1039/D3GC03080F.

33. Zhang, Z. J.; Huang, X.; Chen, X. Y. Polyacrylamide-derived carbon materials: outstanding enhancement of supercapacitor capacitance simply by introducing redox additive of p-aminobenzenesulfonate into KOH electrolyte. *RSC Adv.* **2015**, *5*, 87571–87579, https://doi.org/10.1039/c5ra15484g.

34. Wu, S.; Wei, D.; Cui, H.; Wang, H.; Li Y.; Tao, X.; Yan, C.; Liu, C. Electrochemical performance of polyacrylamide hydrogel based nitrogen-doped porous carbon for supercapacitor. *J. Electroanal. Chem.* **2020**, *865*, 114141, https://doi.org/10.1016/j.jelechem.2020.114141.

35. Chen, X. Y.; Chen, C.; Zhang, Z. J.; Xie, D. H. Nitrogen-doped porous carbon spheres derived from polyacrylamide. *Ind. Eng. Chem. Res.* **2013**, *52*, 12025–12031, https://doi.org/10.1021/ie4017013.

36. Zhang, F.; Liu, H.; Wu, Z.; Zhang, J.; Cui, E.; Yue, L.; Hou, G.; Polyacrylamide gel-derived nitrogen-doped carbon foam yields high performance in supercapacitor electrodes. *ACS Appl. Energy Mater.* **2021**, *4*, 6719–6729, https://doi.org/10.1021/acsaem.1c00777.

37. Yang, Y.; Chen, D.; Han, W.; Cheng, Y.; Sun, B.; Hou, C.; Zhao, G.; Liu, D.; Chen, G.; Han, J.; Zhang, X. Nature-inspired self-activation method for the controllable synthesis of

highly porous carbons for high-performance supercapacitors. *Carbon* **2023**, *205*, 1-9, https://doi.org/10.1016/j.carbon.2023.01.013.

38. Kshetri, T.; Tran, D. T.; Singh, T. I.; Kim, N. H.; Lau, K.; Lee, J. H. Effects of the composition of reduced graphene oxide/carbon nanofiber nanocomposite on charge storage behaviors. *Compos. Part B Eng.* **2019**, *178*, 107500, https://doi.org/10.1016/j.compositesb.2019.107500.

39. Chen, T.; Wang, F.; Cao, S.; Bai, Y.; Zheng, S.; Li, W.; Zhang, S.; Hu, S.-X.; Pang, H. In situ synthesis of MOF-74 family for high areal energy density of aqueous nickel–zinc batteries. *Adv. Mater.* **2022**, *34*, 2201779. https://doi.org/10.1002/adma.202201779.

40. Liu, C.; Bai, Y.; Li, W.; Yang, F.; Zhang, G.; Pang, H. In situ growth of three-dimensional MXene/metal–organic framework composites for high-performance supercapacitors. *Angew. Chem*. **2022**, *61*, e202116282, https://doi.org/10.1002/anie.202116282.

41. Ibrahim, A. G.; Sayed, A. Z.; El-Wahab, H. A.; Sayah, M. M. Synthesis of poly(acrylamide-graft-chitosan) hydrogel: optimization of the grafting parameters and swelling studies. *Am. J. Polym. Sci. Technol.* **2019**, *5*, 55–62, https://doi.org/10.11648/j.ajpst.20190502.13.

42. Lehman, R. L.; Gentry, J. S.; Glumac, N. G. Thermal stability of potassium carbonate near its melting point. *Thermochimica Acta* **1998**, *316*, 1-9, https://doi.org/10.1016/S0040-6031(98)00289-5.

43. Dumitrescu, A. M.; Lisa, G.; Iordan, A. R.; Tudorache, F.; Petrila, I.; Borhan, A. I.; Palamaru, M. N.; Mihailescu, C.; Leontie, L.; Munteanu, C. Ni ferrite highly organized as humidity sensors. *Mater. Chem. Phys.* **2015**, *156*, 170–179, https://doi.org/10.1016/j.matchemphys.2015.02.044.

44. Eguchi, N.; Kawabata, K.; Goto, H. Electrochemical polymerization of polymer liquid crystal solution. *J. Mater. Sci. Chem. Eng.* **2017**, *5*, 64–70, https://doi.org/10.4236/msce.2017.52007.

45. Shrestha, R. L.; Chaudhary, R.; Shrestha, R. G.; Shrestha, T.; Maji, S.; Ariga K.; Shrestha L. K. Washnut seed-derived ultrahigh surface area nanoporous carbons as high rate performance electrode material for supercapacitors. *Bull. Chem. Soc. Jpn.* **2021**, *94*, 565–572, https://doi.org/10.1246/bcsj.20200314.

46. Bairi, P.; Tsuruoka, T.; Acharya, S.; Ji, Q.; Hill, J. P.; Ariga, K.; Yamauchi, Y.; Shrestha, L. K. Mesoporous fullerene C_{70} cubes with highly crystalline frameworks and unusually enhanced photoluminescence properties. *Mater. Horiz.* **2018**, *5*, 285–290, https://doi.org/10.1039/C7MH00954B

47. Villegas, J. P.; Valle, J. F. P.; Rodríguez, J. M. M.; García, M. G. Study of commercial wood charcoals for the preparation of carbon adsorbents. *J. Anal. Appl. Pyrolysis* **2006**, *76*, 103–108, https://doi.org/10.1016/j.jaap.2005.08.002.

48. Shrestha, L. K.; Wei Z.; Subramaniam, G.; Shrestha, R. G.; Singh, R.; Sathish, M.; Ma, R.; Hill, J. P.; Nakamura, J.; Ariga K. Nanoporous hollow carbon spheres derived from fullerene assembly as electrode materials for high-performance supercapacitors. *Nanomaterials* **2023**, *13*, 946, https://doi.org/10.3390/nano13050946.

49. Perez-Calm, A.; Shrestha, L. K.; Magana, J. R.; Esquena, J.; Salonen, L. M.; Shrestha, R. G.; Ma, R.; Ariga, K.; Rodriguez-Abreu, C. Perylene-templated hierarchically porous carbon fibers as efficient supercapacitor electrode material. *Bull. Chem. Soc. Jpn.* **2022**, *95*, 1687–1696, https://doi.org/10.1246/bcsj.20220245.

50. Das, S. K.; Pradhan, L.; Jena, B. K.; Basu, S. Polymer derived honeycomb-like carbon nanostructures for high capacitive supercapacitor application. *Carbon* **2023**, *201*, 49–59, https://doi.org/10.1016/j.carbon.2022.09.004.

51. Sadezky, A.; Muckenhuber, H.; Grothe, H.; Niessner, R.; Pöschl, U. Raman microspectroscopy of soot and related carbonaceous materials: Spectral analysis and structural information. *Carbon* **2005**, *43*, 1731-1742, https://doi.org/10.1016/j.carbon.2005.02.018.

52. Liu, Y.; Wang, S.; Sun, X.; Zhang, J.; uz Zaman F.; Hou L.; Yuan C. Sub-nanoscale engineering of MoO_2 clusters for enhanced sodium storage. *Energy Environ. Mater.* **2023**, *6*, e12263, https://doi.org/10.1002/eem2.12263.

53. Sun, Z.; Liu, Y.; Ye, W.; Zhang, J.; Wang, Y.; Lin, Y.; Hou, L.; Wang, M.-S.; Yuan, C. Unveiling intrinsic potassium storage behaviors of hierarchical NanoBi@N-doped carbon nanocages framework via in situ characterizations. *Angew. Chem.* **2021**, *60*, 7180–7187, https://doi.org/10.1002/anie.202016082

54. Chithra, A.; Wilson, P.; Rajeev, R.; Prabhakaran, K. Nitrogen-doped microporous carbon with high CO_2 sorption by KOH activation of black gram. *Mater. Res. Express* **2018**, *5*, 115606, https://doi.org/10.1088/2053-1591/aade26.

55. Rennie, A. J. R.; Hall, P. J. Nitrogen-enriched carbon electrodes in electrochemical capacitors: investigating accessible porosity using CM-SANS. *Phys. Chem. Chem. Phys.* **2013**, *15*, 16774, https://doi.org/10.1039/c3cp52233d.

56. Guo, D.; Shibuya, R.; Akiba, C.; Saji, S.; Kondo, T.; Nakamura, J. Active sites in nitrogen-doped carbon materials for oxygen reduction reaction clarified using model catalysts. *Science* **2016**, *351*, 361–365, https://doi.org/10.1126/science.aad08

57. Shrestha, L. K.; Shrestha, R. G.; Maji, S.; Pokharel, B. P.; Rajbhandari, R.; Shrestha, R. L.; Pradhananga, R. R.; Hill, J. P.; Ariga, K. High surface area nanoporous graphitic carbon materials derived from lapsi seed with enhanced supercapacitance. *Nanomaterials* **2020**, *10*, 728, https://doi.org/10.3390/nano10040728.

58. Prasankumar, T.; Salpekar, D.; Bhattacharyya, S.; Manoharan, K.; Yadav, R. M.; Mata, M. A. C.; Miller, K. A.; Vajtai, R.; Jose, S.; Roy, S.; Ajayan, P. M. Biomass derived hierarchical porous carbon for supercapacitor application and dilute stream CO_2 capture. *Carbon* **2022**, *199*, 249–257, https://doi.org/10.1016/j.carbon.2022.07.057.

59. Shen, C.; Li, R.; Yan, L.; Shi, Y.; Guo, H.; Zhang, J.; Lin, Y.; Zhang, Z.; Gong, Y.; Niu, L.; Rational design of activated carbon nitride materials for symmetric supercapacitor applications; *Appl. Surf. Sci.* **2018**, *455*, 841–848, https://doi.org/10.1016/j.apsusc.2018.06.065.

60. Liang, Q.; Ye, L.; Huang, Z.-H.; Xu, Q.; Bai, Y.; Kang, F.; Yang, Q.-H. A honeycomb-like porous carbon derived from pomelo peel for use in high-performance supercapacitors. *Nanoscale* **2014**, *6*, 13831–13837, https://doi.org/10.1039/c4nr04541f.

61. Schlee, P.; Hosseinaei, O.; Baker, D.; Landmer, A.; Tomani, P.; Mostazo-Lopez, M. J.; Cazorla-Amorós, D.; Herou, S.; Titirici, M.-M. From waste to wealth: from kraft lignin to free-standing supercapacitors. *Carbon* **2019**, *145*, 470–480, https://doi.org/10.1016/j.carbon.2019.01.035.

62. Song, Y.; Qu, W.; He, Y.; Yang, H.; Du, M.; Wang, A.; Yang, Q.; Chen, Y. Synthesis and processing optimization of N-doped hierarchical porous carbon derived from corncob for high performance supercapacitors. *J. Energy Storage* **2020**, *32*, 101877, https://doi.org/10.1016/j.est.2020.101877.

63. Geng, P. B.; Wang, L.; Du, M.; Bai, Y.; Li, W. T.; Liu, Y. F.; Chen, S. Q.; Braunstein, P.; Xu, Q.; Pang, H. MIL-96-Al for Li–S Batteries: shape or size? *Adv. Mater.* **2022**, *34*, 2107836. https://doi.org/10.1002/adma.202107836.

64. Manikandan, R.; Raj, C. J.; Nagaraju, G.; Velayutham, R.; Moulton, S. E.; Puigdollers, J.; Kim, B. C. Selenium enriched hybrid metal chalcogenides with enhanced redox kinetics for high-energy density supercapacitors. *Chem. Eng. J.* **2021**, *414*, 128924, https://doi.org/10.1016/j.cej.2021.128924.

65. Bhattarai, R. M.; Chhetri, K.; Natarajan, S.; Saud, S.; Kim, S. J.; Mok, Y. S. Activated carbon derived from cherry flower biowaste with a self-doped heteroatom and large specific surface area for supercapacitor and sodium-ion battery applications. *Chemosphere* **2022**, *303*, 135290, https://doi.org/10.1016/j.chemosphere.2022.135290.

66. Nagaraju, G.; Sekhar, S. C.; Ramulu, B.; Hussain, Sk. K.; Narsimulu, D.; Yu, J. S. Ternary MOF-based redox active sites enabled 3D-on-2D nanoarchitectured battery-type electrodes for high-energy-density supercapatteries. *Nano-Micro Lett.* **2021**, *13*, 1–18, https://doi.org/10.1007/s40820-020-00528-9.

67. Magana, J. R.; Kolen'ko, Y. V.; Deepak, F. L.; Solans, C.; Shrestha, R. G.; Hill, J. P.; Ariga K.; Shrestha L. K.; Rodriguez-Abreu C. From chromonic self-assembly to hollow carbon nanofibers: efficient materials in supercapacitor and vapor-sensing applications. *ACS Appl. Mater. Interfaces* **2016**, *8*, 31231–31238, https://doi.org/10.1021/acsami.6b09819.

68. Cai, T.; Yang, Z.; Liu, J.; Xu, K.; Gao, Y.; Zhang, F.; Yang, X.; Xie, M. Carboxymethyl chitosan-derived carbon foam with hierarchical pores tuned by potassium tetraborate and potassium carbonate for supercapacitors. *J. Energy Storage* **2023**, *60*, 106671, https://doi.org/10.1016/j.est.2023.106671.

69. Li, J.; Yun, X.; Hu, Z.; Xi, L.; Li, N.; Tang, H.; Lu, P.; Zhu, Y. Three-dimensional nitrogen and phosphorus co-doped carbon quantum dots/reduced graphene oxide composite aerogels with hierarchical porous structure as superior electrode materials for supercapacitors. *J. Mater. Chem. A* **2019**, *7*, 26311-26325, https://doi.org/10.1039/C9TA08151H.

Table of Contents (TOC) graphic